Applied Geochemistry 100 (2019) 96–103

Contents lists available at ScienceDirect

Applied Geochemistry

journal homepage: www.elsevier.com/locate/apgeochem

Enhanced uptake capacity for uranium(VI) in aqueous solutions by activated natural siderite: Performance and mechanism

Wei Hu[a], Zexin Zhang[a], Mengxue Li[a], Haibo Liu[a,b,*], Changai Zhang[a], Tianhu Chen[a], Yuefei Zhou[a]

[a] Lab for Nano-minerals and Mineral Materials, School of Resources & Environmental Engineering, Hefei University of Technology, Hefei, 230009, China
[b] Institute of Atmospheric Environment & Pollution Control, School of Resources & Environmental Engineering, Hefei University of Technology, Hefei, 230009, China

ARTICLE INFO

Editorial handling by Huaming Guo

Keywords:
Uptake
Siderite
Uranium
XPS analysis
Interaction mechanism

ABSTRACT

Siderite as a Fe(II)-bearing mineral often be naturally weathered and oxidized into goethite, which would decrease the surface chemical activity of the siderite. The chemical activity of siderite is improved by decomposing weathering-formed goethite at low temperature (350 °C). The activated natural siderite (ANS) was utilized to remove U(VI) from aqueous solutions. Batch experiments revealed that ANS after thermal treatment at 350 °C (ANS350) exhibited excellent uptake performance toward U(VI) (14.65 mg/g) which was better than natural siderite (9.00 mg/g) at pH = 4.0 and T = 293 K. Meanwhile, the uptake percents of U(VI) on NS and the uptake process was involved electrostatic attraction on the surface of adsorbents. The characterization results illustrated that activated natural siderite at 350 °C presented the better uptake capacity due to its larger specific surface area and smaller average pore size compared to natural siderite, which was optimized to adsorb U(VI) from aqueous solutions. The spectroscopic analysis demonstrated that the abundant surface oxygenated functional groups of ANS facilitated the uptake process of U(VI). Meanwhile, reduction was also involved in the process. Additionally, the U(VI) reduction amount can be enhanced to some extent after calcination. These findings give insight into the further development of activated natural mineral obtained by heating in low temperature, for using as potential candidate in immobilization of uranium(VI) from contamination water in actual environmental management.

1. Introduction

Over the past last few decades, owing to the mining, extraction, and processing of uranium for nuclear fuel and weapons, there were large amount of long-term nuclear waste had been produced (Sun et al., 2017b; Wang et al., 2017a, 2017b; Zheng et al., 2017). The disposal of this nuclear waste has become a crucial issue, such as uranium, one of the essential nuclear energy sources has been considered as an environmental radioactive pollutant in hydrosphere and biosphere (Lu et al., 2017; Min et al., 2017; Sun et al., 2017a). Uranium has a long radioactive half-life and poses serious toxicity for human beings and ecological balance (Li et al., 2017b; Liu et al., 2017a, 2017b). Moreover, the high mobility of U(VI) in the subsurface would accelerate the food chain transfer of U toxicity (Cheng et al., 2017; Collins and Rosso, 2017). Uranium as a redox sensitive element, its solubility and its mobility depends on its oxidation state: U(VI) can dissolve more easily than U(IV) in groundwater. Thus, the redox of U(VI) can be a excellent method to enrich U(VI) and prevent uranium's transport and migration of U(VI) in the environment. In recent years, Fe-oxides have been extensively demonstrated as potential adsorbents, such as goethite (O'Reilly et al., 2001), hematite (Randall et al., 2001), magnetite (Li et al., 2017c) and siderite (Guo et al., 2007, 2010, 2011). In particular, Fe-bearing mineral containing structural Fe(II), including siderite ($FeCO_3$) (Ithurbide et al., 2010), magnetite (Fe_3O_4) (Ilton et al., 2010; Scheinost and Charlet, 2008), and green rusts (O'Loughlin et al., 2011) which can effectively reduce a wide range of radionuclides (i.e., U(VI), Tc(VII), Np(V), and Se(VI)).

Siderite ($FeCO_3$) is one of the abundant Fe(II)-bearing carbonate mineral naturally present in the geological formations, where it forms a redox buffer with goethite (Guo et al., 2007). It has been found widely distributed in Austria, Russia, China, and Canada (Yang et al., 2018). Especially, there are abundant siderite resources nearly 2 billion in China, but only less than 10% of total reserves had been used (Matthiesen et al., 2013). A number of previous reports have demonstrated that siderite, as a representative secondary Fe(II) mineral, has high chemical activity to enrich contaminants from wastewater or

* Corresponding author. Lab for Nano-minerals and Mineral Materials, School of Resources & Environmental Engineering, Hefei University of Technology, Hefei, 230009, China.
E-mail address: liuhaibosky116@hfut.edu.cn (H. Liu).

https://doi.org/10.1016/j.apgeochem.2018.11.010
Received 25 July 2018; Received in revised form 9 October 2018; Accepted 13 November 2018
Available online 15 November 2018
0883-2927/

drinking water, such as Pb^{2+} (Erdem and Özverdi, 2005), Hg^{2+}(Ha et al., 2017), AsO_4^{3-} (Li et al., 2017a) and $Cr_2O_7^{2-}$ (Erdem et al., 2004). Importantly, under acidic conditions, the carbonates in siderite react with H^+ ions to release Fe^{2+}, which could increase the active sites like hydroxyl groups for ions immobilization (Duckworth and Martin, 2004). A. Ithurbide et al. demonstrated that U(VI) is retained at the siderite surface, reduced and then precipitated as $UO_{2\cdot67}$ at pH 9.0, while iron precipitate into goethite and the uranium retained by the siderite layer and reduced by Fe(II) contained in the thin layer at pH 7.0 (Ithurbide et al., 2010). However, the effect of the surface weathering-formed goethite on the uptake of siderite towards uranium (VI) in containing radionuclides acidic wastewater has been rarely reported.

Herein, natural siderite was activated by calcination for removing uranium from aqueous solutions. The main objectives of this study are (1) to characterize morphology and surface groups of natural siderite (NS) and activated natural siderite (ANS) by using fourier transform infrared spectroscopy (FT-IR), X-ray diffraction (XRD) and X-ray photoelectron spectroscopy (XPS); (2) to investigate the influence of aqueous chemical conditions on U(VI) uptake on NS and ANS using batch experiments; (3) to investigate the effect of weathering-formed goethite on the U(VI) uptake process and the difference in uptake mechanism between NS and ANS towards U(VI) by FT-IR and XPS. This study highlight low temperature activated natural siderite as a promising material for the preconcentration and immobilization of uranium in actual environmental management.

2. Experimental section

2.1. Synthesis of materials

Activated siderite was synthesized by the calcination of natural siderite (Tongling mine of Anhui, China) under atmospheric conditions. Firstly, natural siderite was crushed and sieved to less than 200 mesh using a laboratory mill, the fraction of ≤0.075 mm was used in the study. Afterwards, 1.0 g of natural siderite was placed into the quartz tube, then the power were annealed in air for 1.0 h at different temperatures (200, 250, 300, 350 °C). Thermal treatment was carried out in a tube furnace with a temperature-programmed controller, designing 10 °C/min in this work. To simplify the sample label, ANS350 means adsorbent obtained by thermal treatment of natural siderite at 350 °C. The main mineral compositions were 66.3 wt% of siderite, 22.4 wt% of clay minerals and quartz, 11.3 wt% of goethite. U(VI) stock solution of 1.0×10^{-3} mol/L was prepared by dissolving $UO_2(NO_3)_2$ (spectrographic purity, Sigma-Aldrich) in distilled water and diluting within 0.1 mo/L $HClO_4$ solution. Other reagents used in these experiments were of analytical grade, and all the solutions were prepared with distilled water.

2.2. Characterization

The morphologies were performed by using transmission electron microscopy (Philips JSM-6490LV). Mineral composition was determined by X-ray diffraction analysis (Dandonghaoyuan 2700), using Cu Kα radiation. The BET surface area of siderite was calculated by Novawin 3000e Surface Area. The zeta potentials of the materials were obtained as a function of pH by Malvern Zetasizer Nano-ZS at 293 K. The function groups were demonstrated conducted by FT-IR measurement (VERTEX-70). XPS analyses were conducted with a Thermo Escalab 250 electron spectrometer using Al Kα X-ray source. The recorded data, U *4f*, Fe *2p*, O *1s* and C *1s*, were fitted with the XPSPEAK41 mode using a Lorentzian–Gaussian peak shape and a shirley background was used.

2.3. Batch experiments

The batch experiments to study the uptake of U(VI) as a function of pH, reaction time and solution concentration were conducted with a solid-to-liquid ratio of 1.0 g/L and 20.0 mg/L U(VI) at T = 293 K in the presence of 0.01 mol/L $NaClO_4$. The initial pH was adjusted from 3.0 to 10.0 with 0.001–0.1 mol/L $HClO_4$ or NaOH solution. The uptake kinetics of U(VI) on siderite were reacted for different time ranging from 5 min to 24 h with continuous stirring rotator. The uptake kinetics and isotherms were conducted at pH = 4.0 ± 0.1 at different times and initial concentration of U(VI). After reaction for 24 h to achieve equilibrium, the suspensions centrifuged at 4500 × g for 10 min then filtered through a 0.22-μm membrane. The control experiments were also performed to test the effect of the sorption on the tube walls during the reaction process. All experimental data were the average of triplicate determinations and the relative errors were within ± 5%.

The residual concentration of U(VI) in aqueous solutions counting on a kinetic phosphorescence analyzer (KPA-11, Richland, USA). The concentration of the U species was expressed as the element (U). The uptake percentage (sorption, %) and uptake capacity (Q_e, mg/g) can be expressed as Eqns. (1) and (2), respectively:

$$\text{Sorption } (\%) = (C_0 - C_e) / C_0 \times 100\% \quad (1)$$

$$Q_e = V \times (C_0 - C_e) / m \quad (2)$$

where C_0 and C_e (mg/L) are original and equilibrated concentration after reaction, respectively. m (g) and V (L) are the mass of adsorbent and the suspension volume, respectively.

3. Results and discussion

3.1. Characterization

As shown in Fig. 1A, natural siderite displayed typically rhombic-like morphology and relatively rough surface with small cracks (Guo et al., 2007; Yang et al., 2018). It is noted that the natural siderite was mainly covered by of shoots-like and radial goethite agglomeration (O'Reilly et al., 2001). The goethite tightly nested on the siderite, which drastically limited surface active chemical activity of siderite. The XRD patterns of activated natural siderite were displayed in Fig. 1B, the reflections of siderite at 2θ = 24.8, 32.0, 38.3, 42.3, 46.2, 50.8, 52.6, 61.5° can be found. However, the peak at 2θ of 21.2, 36.7, 33.2° were indexed to (110), (111) and (130) plane of goethite, while peaks at 26.6° corresponded to the (011) planes of quartz (Yang et al., 2018; Zhang et al., 2018). It is evident that NS is composed of siderite, goethite and quartz mixture phases. These characteristic reflections of goethite (FeOOH) completely disappeared and which were transformed into hematite (α-Fe_2O_3) when the thermal treatment temperature was up to 350 °C (Liu et al., 2013). The transformation can take place as given in Eqn. (3).

$$2FeOOH = Fe_2O_3 + H_2O \quad (3)$$

As shown in Table 1, the surface area of series of materials increased with the increasing heating temperature. The thermal decomposition of FeOOH forming nano-porous Fe_2O_3 was previously reported. The SSA of natural siderite was 18.62 m^2/g and ANS350 presented a maximum surface area of 33.06 m^2/g, which would be attributed to the formation of micropores (1.67–2.18 nm) owing to the dehydroxylation of goethite (Fig. 1C) (Li et al., 2017c). Liu et al. also demonstrated the surface area significantly increased from 12.7 to the maximum of 111.6 m^2/g when the temperature increased to 350 °C, which was ascribed to the decomposition of natural goethite into hematite by dehydrogenation (Liu et al., 2013). It was observed that pores existed mainly in the form of mesopores (2–10 nm), and the number of mesopores gradually increased with the increasing heating temperature. The average pore size (5.68 nm) of ANS350 decreased compared to natural siderite (9.65 nm). The larger specific surface area can be optimized to adsorb U(VI) from aqueous solutions due to provide more surface active sites (Madhavi et al., 2013). As presented in Fig. 1D, the pHpzc (pH at point of zero

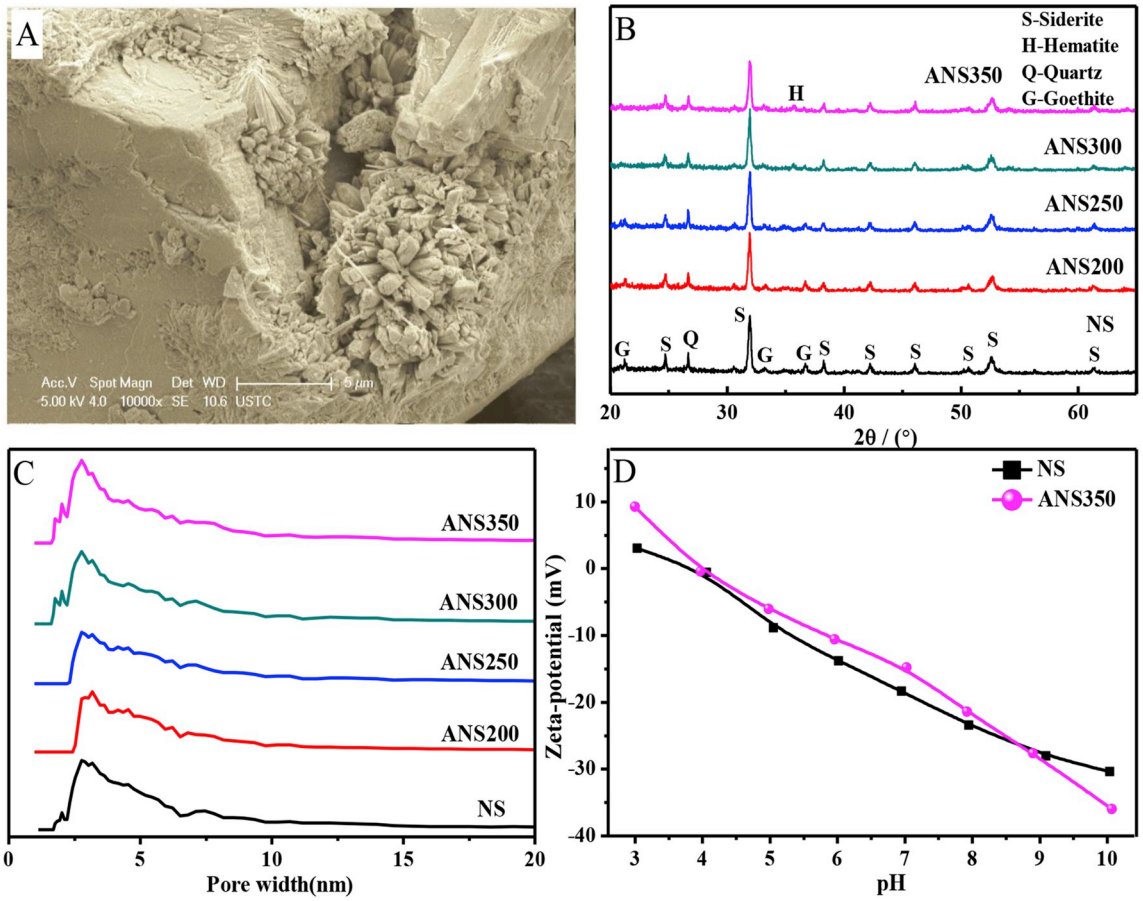

Fig. 1. SEM image of natural siderite (A), XRD patterns of NS and ANS (B), pore size distributions of NS and ANS (C), zeta potential values of NS and ANS350, m/V = 1.0 g/L, T = 293 K (D).

Table 1
Specific surface area, pore volume and average pore size.

Sample	BET (m2/g)	Pore volume (cm3/g)	Average pore size (nm)
NS	18.62	0.045	9.65
ANS200	16.73	0.036	8.61
ANS250	18.14	0.035	7.81
ANS300	28.83	0.044	6.16
ANS350	33.06	0.047	5.68

charge) values of NS and ANS350 were ~3.9 and 4.1, respectively. The surface charge was favorable to bind the positively charged U(VI) species at pH > pHpzc.

3.2. Uptake kinetics

The U(VI) uptake kinetic experiment was carried out with initial U (VI) concentration of 20.0 mg/L at 293K. The time-dependent uptake of U(VI) on NS and ANS350 were depicted in Fig. 2A. Fig. 2B and C showed the simulation of two linear adsorption kinetics models. The uptake amount of U(VI) on ANS350 were significantly higher than that of NS. The activated siderite possesses the larger surface area and more porous structure, which provided more reactive sites and hence improves the uptake capacity. The uptake rate of U(VI) on ANS350 and NS rapidly increased at first 120 min, after that, the rate gradually tends to be gentle. One can be seen that the equilibrium was reached within 1440 min, the uptake efficiency of U(VI) on NS and ANS350 reached to 38.1% and 57.3%, respectively. To achieve the reaction equilibrium, the following experiments employed 24 h as reaction time. Hence, to further understand the interaction mechanism and its potential rate-controlling steps, the experimental data were simulated by pseudo-second-order and pseudo-first-order kinetic models (Erdem et al., 2004; Guo et al., 2010). Their linear forms were expressed as following:

$$\ln (C_0 - C_e) = \ln (Q_e) - K_1 \times t \quad (4)$$

$$t / Q_t = 1 / (K_2 \times Q_e^2) + t / Q_e \quad (5)$$

where Q_t and Q_e (both in mg/g) are the uptake amounts of U(VI) at time t (min) and at equilibrium time, respectively. K_1 (1/min) and K_2 (g/(min ·mg)) are the rate constants of the pseudo-first-order and the pseudo-second-order kinetic models, respectively. The fitted parameters were tabulated in Table 2. It is clear that the observed Qe values (the uptake amounts of U(VI) at equilibrium time) on NS and ANS350 (7.57 and 11.34 mg/g) were well closer to the theoretical value calculated from pseudo-second order kinetic model (1.96 and 4.39 mg/g) compared to pseudo-first order (7.63 and 11.46 mg/g). The uptake kinetics indicated the rate-limiting step for U(VI) uptake on NS and ANS350 were chemisorptions (Cheng et al., 2017; Sun et al., 2012b).

3.3. Effect of initial pH

The effects of initial solution pH on U(VI) uptake on NS and ANS350 were investigated at the pH ranging from 3.0 to 9.0. As depicted in Fig. 3A and Fig. 3B, it shows that NS and ANS350 adsorbed U(VI) efficiently in a relatively wide pH range, although U(VI) uptake efficiency was higher in alkaline conditions than that in acidic conditions. The uptake trends of U(VI) on the two materials were similar, and the sorption curves contained three parts. The uptake of U(VI) onto NS and ANS350 drastically increased with increasing pH from 4.0 to 6.0, then remained relatively high uptake rate (~100%) at pH 6.0–8.0 for NS

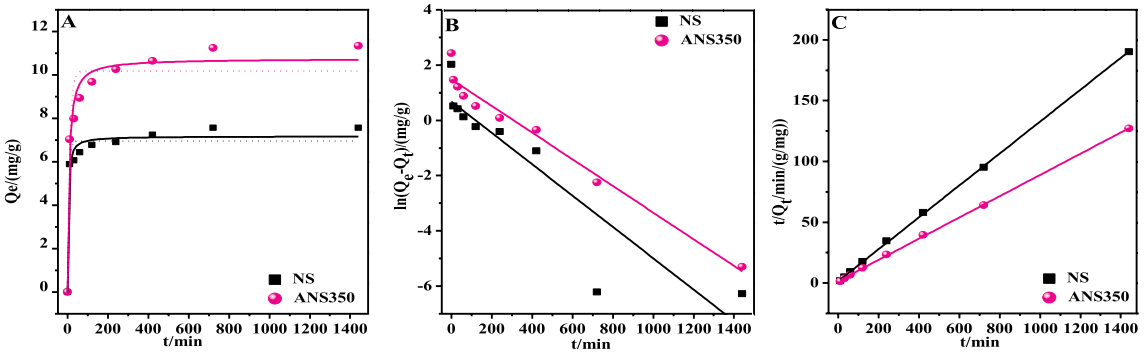

Fig. 2. (A) Uptake kinetics of U(VI) on NS and ANS350 (The dashed lines represent the pseudo-first-order model), (B)pseudo-first-order model, (C)pseudo-second-order model. C(UO_2^{2+}) = 20 mg/L, m/V = 1.0 g/L, I = 0.01 mol/L $NaNO_3$, T = 293 K, pH = 4.0.

Table 2
Parameters of pseudo-first-order and pseudo-second-order kinetic models.

Adsorbents	Pseudo-first-order			Pseudo-second-order		
	Q_e (mg/g)	K_1 (1/min)	R^2	Q_e (mg/g)	K_2 (g/(min·mg))	R^2
NS	1.9636	0.005	0.8091	7.6278	0.0103	0.9997
ANS350	4.3938	0.004	0.9643	11.4587	0.0005	0.9997

and pH 6.0–7.5 for ANS350, whereas the uptake amount of U(VI) on NS and ANS350 decreased at pH > 8.0 at the initial concentration of 20 mg/L. The uptake curves could be described by the surface property of NS/ANS350 and relative distribution of U(VI) in solution at different pH values. The relative species of U(VI) in aqueous solutions at different pH values was exhibited in Fig. 3C. It is clear noted that U(VI) mainly present the form of positive species (e.g., UO_2^{2+}, UO_2OH^+, $(UO_2)_2(OH)_2^{2+}$, and $(UO_2)_3(OH)_5^+$) at pH < 6.0 (Shuibo et al., 2009; Sun et al., 2016a). Thus, the high uptake efficiency of uranium at pH < 6.0 was mainly attributed to the strong electrostatic attraction between the positive species of uranium and negatively charged surface of NS/ANS350 enhanced surface complexation interactions. The high uptake percentage (~100%) of U(VI) at pH > 6.0 was due to the formation of the chemical precipitation (schoepite). However, carbonato-uranyl complexes (e.g., $(UO_2)_3(CO_3)_2^{2-}$ and $(UO_2)_3(CO_3)_3^{4-}$) were the major species of U(VI) at alkaline condition, which inhibited the binding of the negatively charged U(VI) species to the negatively charged surface of NS/ANS350 owing to electrostatic repulsion (Ding et al., 2015b; Sun et al., 2017b). The uptake tendency of U(VI) on NS/ANS350 was accounted for synergistic effect including electrostatic interaction, surface complexation and chemical precipitation. In addition, equilibrium pH values at different initial pH were also shown in Fig. 3A and B. Except for the batch at pH 3.0–4.0, equilibrium solutions maintain a neutral pH around 6.6 when U(VI) reacted with ANS350 with initial pH range from 4.0 to 9.0. The protonation and deprotonation equilibria of Fe-oxides were involved during the experiments (Fox et al., 2013; Kholodov and Butuzova, 2008; Scott et al., 2005), which can be written as Eqns (4) and (5):

$$\equiv FeOH + H^+ \Leftrightarrow \equiv FeOH_2^+ \quad (4)$$

$$\equiv FeOH \Leftrightarrow \equiv FeO^- + H^+ \quad (5)$$

The pHpzc (pH at point of zero charge) of ANS350 was ~4.1, the species on the ANS350 surface was $\equiv FeOH_2^+$ when pH < 4.1 whereas the species was $\equiv FeO^-$ at pH > 4.1. The solution pH increased after reaction with initial pH 3.0–5.0, which likely due to the continuous ligand exchange between surface -OH groups or Fe-O groups and UO_2^{2+} (Zhao and Guo, 2014).

3.4. Uptake capacity

Uptake isotherms not only can be used to quantify the uptake capacity, but also provide crucial information to understand the reaction process. The uptake isotherms of U(VI) on the three adsorbents were illustrated in Fig. 4A. To further understand the interaction of U(VI) on the three adsorbents and quantify experimental data, two well-known isotherm models (Sun et al., 2012a; Wang et al., 2016; Zhao et al., 2016) (i.e., the Langmuir and Freundlich) were introduced to describe the experimental data, which were expressed by Eqns. (6) and (7):

$$C_e / Q_e = 1 / (K_L \times Q_m) + C_e / Q_m \quad (6)$$

$$\ln Q_e = 1/n \times \ln C_e + \ln K_F \quad (7)$$

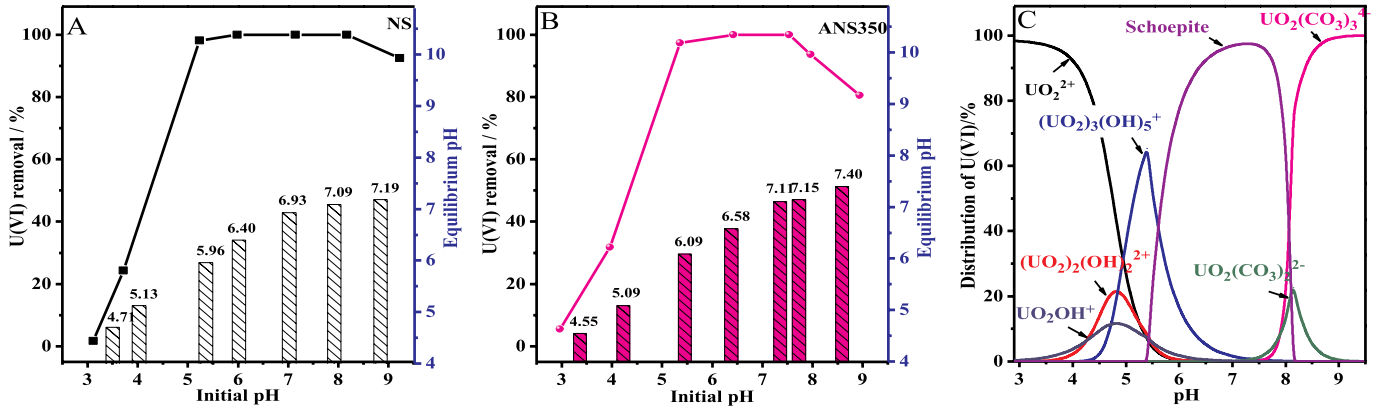

Fig. 3. Influence of initial pH on U(VI) uptake onto NS (A) and ANS350 (B), (C): Distribution of U(VI) species in aqueous solutions, C(UO_2^{2+}) = 20 mg/L, m/V = 1.0 g/L, I = 0.01 mol/L $NaNO_3$, T = 293 K, pH = 4.0.

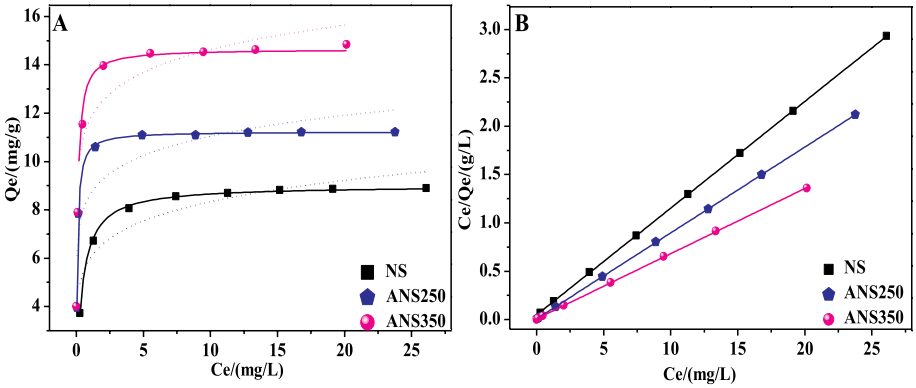

Fig. 4. A: Fitting of U(VI) uptake on NS, ANS250 and ANS350 (The solid lines represent the Langmuir model) (A), the fitting of uptake isotherms of U(VI) on ANS350 by Langmuir model (B). C(UO_2^{2+}) = 4–35 mg/L, m/V = 1.0 g/L, I = 0.01 mol/L $NaNO_3$, T = 293 K, pH = 4.0.

Table 3
Parameters of Langmuir and Freundlich isotherm models.

Adsorbents	Langmuir			Freundlich		
	Q_m (mg/g)	K_L (L/mg)	R^2	K_F ($mg^{1-n}\cdot L^n/g$)	*1/n*	R^2
NS	9.00	0.33	0.9972	5.97	0.145	0.8600
ANS250	11.24	1.06	0.9987	8.60	0.109	0.8224
ANS350	14.65	1.81	0.9800	11.73	0.096	0.8323

where Q_m (mg/g) represents the maximum uptake capacity, and K_L (L/mg) is the Langmuir constant which is related to the free energy of sorption. K_F ($mg^{1-n}\cdot L^n/g$) represents the equilibrium coefficient. *n* is relevant to the uptake intensity at particular temperature. Fig. 4 and Table 3 show the simulated results. Fig. 4A shows the typical isotherms of U(VI) sorption on NS, ANS250 and ANS350. On the basis of the experimental results, the maximum uptake capacity of NS and ANS350 were 9.00 and 11.22 mg/g which suggested the uptake isotherms herein were simulated better by Langmuir model. Particularly, ANS350 showed a more intensive sorption capability of U(VI) than ANS250 (11.24 mg/g) and NS (9.00 mg/g). It could be clearly found that the correlation coefficients of Langmuir model were much higher than Freundlich model which revealed the elimination of U(VI) on siderite particles was a homogeneous process and almost monolayer coverage (Hu et al., 2017; Sun et al., 2017b). As depicted in Table 4, the maximum uptake capacity (14.65 mg/g) of U(VI) on the ANS350 was significant higher than some iron oxides such as nanomagnetite synthesized by calcination (2.46 mg/g) (Li et al., 2017c), collosol hematite (3.36 mg/g) (Xie et al., 2009), and some natural materials (natural zeolite (Misaelides et al., 1995), alumina (Sylwester et al., 2000) and sericite (Sun et al., 2016b)) which indicated that ANS350 could be a economic material to remove radioactive U(VI) from real wastewater.

3.5. Interaction mechanism

FT-IR and XPS technique are widely used to analyze the interaction mechanism. In the FT-IR spectra (Fig. 5A), the broad band in the range of > 1800 cm^{-1}, such as the broad peak at 3422 cm^{-1} was assigned to the stretching vibration of Si-OH and the -OH stretching vibrations (3618 cm^{-1}) were present in NS (Li et al., 2017b; Worasith et al., 2011). For NS spectrum, the peaks at 474 and 536 cm^{-1} corresponded to Si-O bending vibration strongly overlap with infrared active modes of goethite, the peaks became broader in ANS350 due to the influence of the fundamental vibrations of hematite (at 350 and 580 cm^{-1}) after calcination (Tang et al., 2011; Zhao and Guo, 2014). The broad peak at ~1045 cm^{-1} was ascribed to Si-O stretching vibration in clay minerals. The peak at 2978 cm^{-1} due to the characteristic band of goethite and the band was diminished after calcination. Moreover, the peaks at 864 and 1416 cm^{-1} were attributed to the bending and stretching vibration of -CO_3, respectively (Zhao and Guo, 2014). The peaks of -CO_3 in ANS 350 almost had no obvious change compared to NS. These observations implied that goethite completely transformed into hematite, and the siderite structure did not change.

For U-loaded sample, the occurrence of the distinct peak at 908 cm^{-1} around 550–1000 cm^{-1} region can be assigned to antisymmetric vibration of O=U=O and stretching vibrations of weekly bonded oxygen ligands with uranium (U–O_{ligand}) (Tian et al., 2011). The relative intensities of characteristic band of NS-U at 474 cm^{-1} was significantly higher than that of NS, and the absorption band of -CO_3 (864 cm^{-1}) was slightly shifted and the intensity enhanced. The relative intensities of Si-O stretching vibrations at 1045 cm^{-1} for NS-U and Si-OH band at 3422 cm^{-1} for ANS350-U significantly increased after U(VI) uptake, which indicating the hydroxyl groups were responsible for U(VI) uptake onto materials (Chen et al., 2016).

XPS spectra were further employed to investigate the chemical composition and oxidation state. From the survey spectra (Fig. 5B), the main elements of NS and ANS350 were U, C, O and Fe. Fig. 5C shows the spectrum of the U *4f*, U *4f* spectrum displayed two splitting peaks centred on 382.0 and 392.0 eV for U $4f_{7/2}$ (382.1 eV) and U $4f_{5/2}$ (392.8 eV), respectively (Liu et al., 2009). Each peak could be deconvoluted into two individual peak, indicative of two different oxidation states such as 381.3 and 382.3 eV, corresponding to U(IV) and U(VI), suggesting that the adsorbed U(VI) was partially reduced to sparingly soluble U(IV) during the U(VI) uptake process in solutions, which was

Table 4
Comparison of uptake capacities of U(VI) on various natural materials.

Adsorbents	Exp. conditions	Q_m (mg/g)	Reference
Nanomagnetite	pH 2.5, 293 K	2.46	(Li et al., 2017c; Misaelides et al., 1995; Sun et al., 2016b; Sylwester et al., 2000; Xie et al., 2009)
Hematite	pH n.a, 293 K	3.36	Xie et al. (2009)
Natural zeolite material	pH 2.8, 293 K	8.70	Misaelides et al. (1995)
Alumina	pH 6.5, n.a K	9.95	Sylwester et al. (2000)
Sericite	pH 5.0, 293 K	21.41	Sun et al. (2016b)
ANS350	pH 4.0, 293 K	14.65	This work

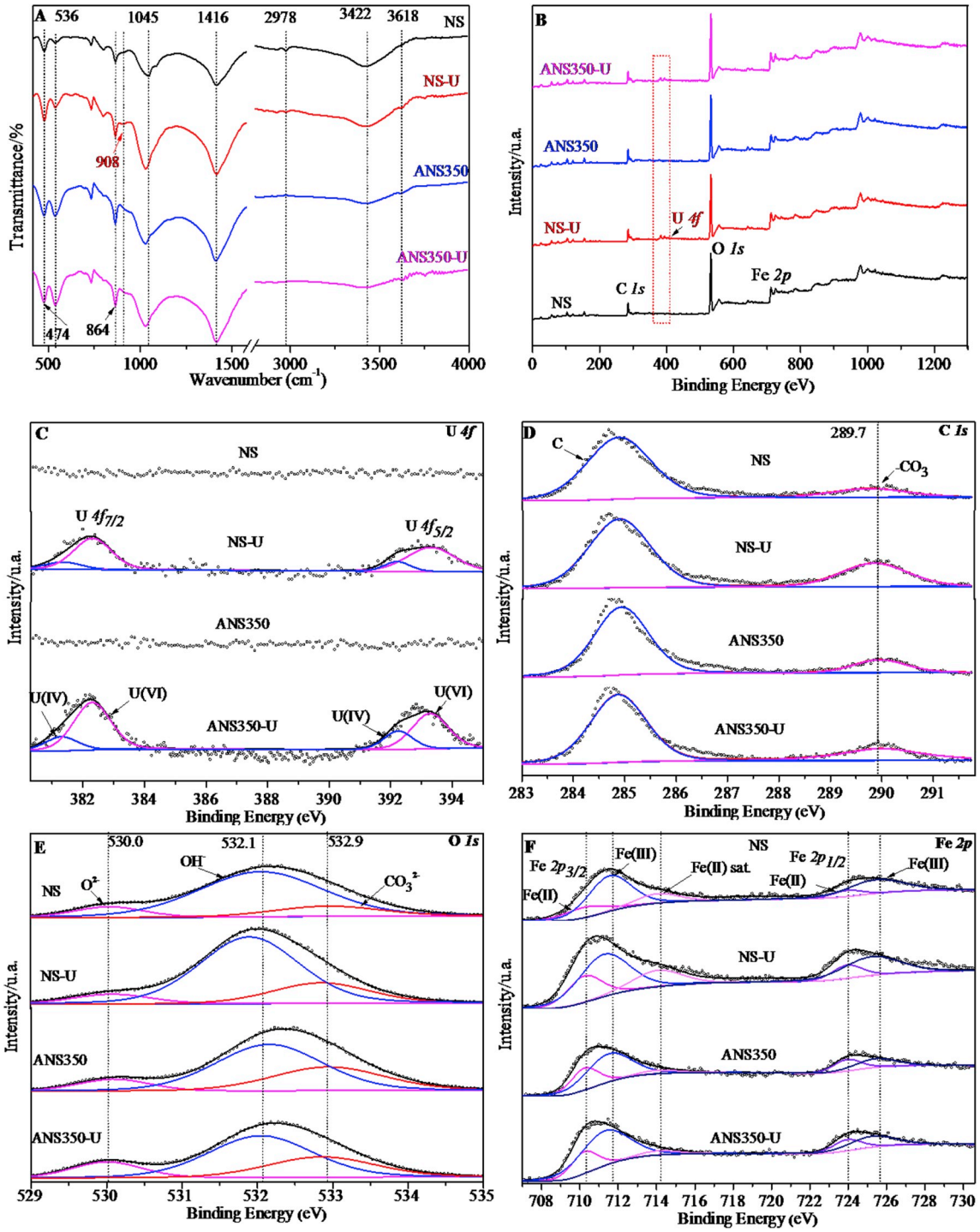

Fig. 5. FT-IR spectra of NS and ANS (A), XPS spectra survey and high resolution scans of NS and ANS before and after U(VI) uptake, total survey scans (B), high resolutions of U *4f*, C *1s*, O *1s* and Fe *2p*, respectively (C–F). C(UO_2^{2+}) = 20 mg/L, m/V = 1.0 g/L, I = 0.01 mol/L $NaNO_3$, T = 293 K, pH = 4.0.

consistent with the results reported by A. Ithurbide (Ithurbide et al., 2010). It can be clearly observed that calcination can enhance the U(VI) reduction amount to some extent. The C *1s* peaks (Fig. 5D) can be distributed into two main components at 284.9 and 289.7 eV, which were attributed to the hydrocarbons adsorbed on the samples and -CO_3 of siderite, respectively (Heuer and Stubbins, 1999; Ithurbide et al., 2009). It is interesting to note that the relative intensity of -CO_3 for NS-U was higher than that of NS, which indicated that the goethite and siderite may be separated due to hydration and natural factors in acidic condition.

The high resolution scans of O *1s* spectrum reveals three major peaks centered at 530.0, 532.0 and 532.5 eV, which were corresponded to the O^{2-} (hematite, goethite), OH^- (goethite, surface adsorbed hydroxyl species) and CO_3^{2-} (siderite) found in the mineral standards, respectively (Duckworth and Martin, 2004; Heuer and Stubbins, 1999). Generally, the existence of oxygen-containing functional groups has positive impact to promote the uptake process. Li et al. demonstrated that a high effective sorption of U(VI) at low pH conditions ascribed to the oxygenated functional groups of nanomagnetite (Li et al., 2017c). Zhang et al. studied the sorption of Hg(II) on α-Fe_2O_3 and found the process could be primarily attributed to hydroxyl groups on the surface of α-Fe_2O_3 (Zhang et al., 2018). Furthermore, Li et al. found the inner-

sphere complexation of U(VI) with oxygen-containing functional group at pH 4.0 according to the XPS results (Li et al., 2018). As shown in Fig. 5E, the binding energy of O *1s* changed in some extent after uptake. It was easy to find that the peak positions of OH^- for NS-U and ANS350-U significantly shifted to lower binding energies, which illustrated that U(VI) removal were attributed to chemisorbed OH^- groups. The relative intensities of carbonate for NS-U were significantly higher than intensities of NS while there was almost no change for ANS350-U which was in good agreement with the FT-IR spectra. In addition, the peak intensity of O^{2-} for ANS350 increased while the intensity of OH^- slightly decreased after U(VI) uptake, indicating U(VI) uptake on ANS350 mainly by hydroxyl groups. This result further demonstrated that U(VI) might form surface complexation with oxygenated functional groups in the whole experimental processes.

In the high resolution Fe *2p* spectrum (Fig. 5F), the two double peaks were attributed to the Fe $2p_{3/2}$ peak (at ~711.6 eV) and Fe $2p_{1/2}$ peak (at ~724.6 eV), respectively (Ding et al., 2015a; Liu et al., 2017a). The Fe $2p_{3/2}$ peaks and Fe $2p_{1/2}$ peaks were clearly deconvoluted into the siderite Fe(II) located at 710.2 and 723.9 eV and the Fe(III) compound one located at 711.5 and 725.4 eV, accompanied with the shake-up satellites (at 714.0 eV). After U(VI) uptake, the increase in relative intensity of Fe(II) peak (at 710.2 eV) for NS-U could due to the separation between goethite and siderite. Meanwhile, the binding energies of Fe(III) peaks for NS-U and ANS350-U shifted to the lower energies which attributed to the uptake of U(VI). In addition, a slight increase in relative intensities of Fe(III) was observed for ANS350-U, which was corresponded to the partly oxidation of Fe(II) to Fe(III) during the uptake process (H. et al., 2005; Ilton et al., 2010). Uptake reactions are controlled by the amount of surface sites of the minerals used. The efficient uptake capacity of ANS350 could be attributed to the simultaneous adsorption and reduction. Based on the above analysis, the enhanced uptake amount of U(VI) at low pH conditions probably ascribed to the increased metal oxygen-containing groups and the contact area of ferric iron.

4. Conclusions

In summary, activated natural siderite, as a bi-mineral adsorbent, was directly synthesized by heating natural siderite under air condition in this study. The weathering-formed goethite completely converted to hematite. Kinetics data revealed that U(VI) uptake on ANS350 and NS were fitted perfectly with pseudo-second-order kinetics and the chemisorptions was the main mechanism for U(VI) uptake on ANS350 and NS. The batch experimental results indicated that ANS350 displayed outstanding uptake capacity toward U(VI) (14.65 mg/g, pH = 4.0, T = 293 K) compare to natural siderite (9.00 mg/g) estimated from Langmuir model. The elimination process of U(VI) on ANS350 and NS were strongly dependent on initial pH. Concluded from FT-IR and XPS analysis, the disappearance of the surface goethite enhanced the uptake efficiency and reduction amount, which could be ascribed to the increased oxygenated functional groups (i.e., Fe-O) after calcinations and the contact area of reactive sites. From the simple activated method and high uptake capacity, ANS350 could be used an ideal adsorbent for the preconcentration and elimination of radionuclides from large volumes of wastewater in practical engineering.

Acknowledgments

Financial supports from National Natural Science Foundation of China (No. 41772038, 41572029), the Fundamental Research Funds for the Central Universities (JZ2017HGTB0196) are acknowledged.

Appendix A. Supplementary data

Supplementary data to this article can be found online at https://doi.org/10.1016/j.apgeochem.2018.11.010.

References

O'Loughlin, E.J., Boyanov, M.I., Antonopoulos, D.A., Kemner, K.M., 2011. Redox processes affecting the speciation of technetium, uranium, neptunium, and plutonium in aquatic and terrestrial environments. ACS Symp. Ser. 1071, 477–517.
Chen, L., Zhao, D., Chen, S., Wang, X., Chen, C., 2016. One-step fabrication of amino functionalized magnetic graphene oxide composite for uranium(VI) removal. J. Colloid Interface Sci. 472, 99–107.
Cheng, W.C., Ding, C.C., Wu, Q.Y., Wang, X.X., Sun, Y.B., Shi, W.Q., Hayat, T., Alabadi, A., Chai, Z.F., Wang, X.K., 2017. Mutual effect of U(VI) and Sr(II) on graphene oxides: evidence from EXAFS and theoretical calculations. Environ. Sci.: Nano 4, 1124–1131.
Collins, R.N., Rosso, K.M., 2017. Mechanisms and rates of U(VI) reduction by Fe(II) in homogeneous aqueous solution and the role of U(V) disproportionation. J. Phys. Chem. A 121, 6603–6613.
Ding, C.C., Cheng, W.C., Sun, Y.B., Wang, X.K., 2015a. Effects of *Bacillus subtilis* on the reduction of U(VI) by nano-Fe^0. Geochim. Cosmochim. Acta 165, 86–107.
Ding, C.C., Cheng, W.C., Sun, Y.B., Wang, X.K., 2015b. Novel fungus-Fe_3O_4 bio-nanocomposites as high performance adsorbents for the removal of radionuclides. J. Hazard Mater. 295, 127–137.
Duckworth, O.W., Martin, S.T., 2004. Role of molecular oxygen in the dissolution of siderite and rhodochrosite 1. Geochim. Cosmochim. Acta 68, 607–621.
Erdem, M., Özverdi, A., 2005. Lead adsorption from aqueous solution onto siderite. Separ. Purif. Technol. 42, 259–264.
Erdem, M., Gur, F., Tumen, F., 2004. Cr(VI) reduction in aqueous solutions by siderite. J. Hazard Mater. 113, 217–222.
Fox, P.M., Davis, J.A., Kukkadapu, R., Singer, D.M., Bargar, J., Williams, K.H., 2013. Abiotic U(VI) reduction by sorbed Fe(II) on natural sediments. Geochim. Cosmochim. Acta 117, 266–282.
Guo, H., Stuben, D., Berner, Z., 2007. Adsorption of arsenic(III) and arsenic(V) from groundwater using natural siderite as the adsorbent. J. Colloid Interface Sci. 315, 47–53.
Guo, H., Li, Y., Zhao, K., 2010. Arsenate removal from aqueous solution using synthetic siderite. J. Hazard Mater. 176, 174–180.
Guo, H., Li, Y., Zhao, K., Ren, Y., Wei, C., 2011. Removal of arsenite from water by synthetic siderite: behaviors and mechanisms. J. Hazard Mater. 186, 1847–1854.
H, J.B., A, D.B., D, B.W., 2005. Chemical reduction of U(VI) by Fe(II) at the solid − water interface using natural and synthetic Fe(III) oxides. Environ. Sci. Technol. 39, 5642–5649.
Ha, J., Zhao, X., Yu, R., Barkay, T., Yee, N., 2017. Hg(II) reduction by siderite (FeCO 3). Appl. Geochem. 78, 211–218.
Heuer, J.K., Stubbins, J.F., 1999. An XPS characterization of $FeCO_3$ films from CO_2 corrosion. Corrosion Sci. 41, 1231–1243.
Hu, B.W., Hu, Q.Y., Chen, C.G., Sun, Y.B., Xu, D., Sheng, G.D., 2017. New insights into Th (IV) speciation on sepiolite: evidence for EXAFS and modeling investigation. Chem. Eng. J. 322, 66–72.
Ilton, E.S., Boily, J.F., Buck, E.C., Skomurski, F.N., Rosso, K.M., Cahill, C.L., Bargar, J.R., Felmy, A.R., 2010. Influence of dynamical conditions on the reduction of U(VI) at the magnetite-solution interface. Environ. Sci. Technol. 44, 170–176.
Ithurbide, A., Peulon, S., Miserque, F., Beaucaire, C., Chaussé, A., 2009. Interaction between uranium(VI) and siderite ($FeCO_3$) surfaces in carbonate solutions. Radiochim. Acta 97.
Ithurbide, A., Peulon, S., Miserque, F., Beaucaire, C., Chaussé, A., 2010. Retention and redox behaviour of uranium(VI) by siderite ($FeCO_3$). Radiochim. Acta 98, 563–568.
Kholodov, V.N., Butuzova, G.Y., 2008. Siderite formation and evolution of sedimentary iron ore deposition in the Earth's history. Geol. Ore Deposits 50, 299–319.
Li, F., Guo, H., Zhou, X., Zhao, K., Shen, J., Liu, F., Wei, C., 2017a. Impact of natural organic matter on arsenic removal by modified granular natural siderite: evidence of ternary complex formation by HPSEC-UV-ICP-MS. Chemosphere 168, 777–785.
Li, M., Liu, H., Chen, T., Lin, W., 2017b. Nano-hematite prepared by activation of natural siderite and its performance on immobilization of Eu(III). Appl. Geochem. 84, 154–161.
Li, M.X., Sun, Y.B., Liu, H.B., Chen, T.H., Hayat, T., Alharbi, N.S., Chen, C.L., 2017c. Spectroscopic and modeling investigation of Eu(III)/U(VI) sorption on nanomagnetite from aqueous solutions. ACS Sustain. Chem. Eng. 5, 5493–5502.
Li, M., Liu, H., Chen, T., Dong, C., Sun, Y., 2018. Synthesis of magnetic biochar composites for enhanced uranium(VI) adsorption. Sci. Total Environ. 651, 1020–1028.
Liu, J.H., Berghe, S.V.D., Konstantinović, M.J., 2009. XPS spectra of the U5 + compounds KUO_3KUO_3, $NaUO_3NaUO_3$ and $Ba_2U_2O_7$. J. Solid State Chem. 5, 1105–1108.
Liu, H., Chen, T., Zou, X., Qing, C., Frost, R.L., 2013. Thermal treatment of natural goethite: thermal transformation and physical properties. Thermochim. Acta 568, 115–121.
Liu, H.B., Li, M.X., Chen, T.H., Chen, C.L., Alharbi, N.S., Hayat, T., Chen, D., Zhang, Q., Sun, Y.B., 2017a. New synthesis of nZVI/C composites as an efficient adsorbent for the uptake of U(VI) from aqueous solutions. Environ. Sci. Technol. 51, 9227–9234.
Liu, H.B., Zhu, Y.K., Xu, B., Li, P., Sun, Y.B., Chen, T.H., 2017b. Mechanical investigation of U(VI) on pyrrhotite by batch, EXAFS and modeling techniques. J. Hazard Mater. 322, 488–498.
Lu, S.H., Hu, J.S., Chen, C.L., Chen, X.J., Gong, Y., Sun, Y.B., Tan, X.L., 2017. Spectroscopic and modeling investigation of efficient removal of U(VI) on a novel magnesium silicate/diatomite. Separ. Purif. Technol. 174, 425–431.
Chemistry, D.O., University, S.V., ApMadhavi, V., Reddy, A.V.B., Reddy, K.G., 2013. An overview on research trends in remediation of chromium. Res. J. Recent Sci. 2, 71–83.
Matthiesen, H., Hilbert, L.R., Gregory, D.J., 2013. Siderite as a corrosion product on archaeological iron from a waterlogged environment. Stud. Conserv. 48, 183–194.

Min, X., Yang, W., Hui, Y.-F., Gao, C.-Y., Dang, S., Sun, Z.-M., 2017. Fe_3O_4@ZIF-8: a magnetic nanocomposite for highly efficient UO_2^{2+} adsorption and selective UO_2^{2+}/Ln^{3+} separation. Chem. Commun. 53, 4199–4202.
Misaelides, P., Godelitsas, A., Filippidis, A., Charistos, D., Anousis, I., 1995. Thorium and uranium uptake by natural zeolitic materials. Sci. Total Environ. 173–174, 237–246.
O'Reilly, S.E., Strawn, D.G., Sparks, D.L., 2001. Residence time effects on arsenate adsorption/desorption mechanisms on goethite. Soil Sci. Soc. Am. J. 65, 67–77.
Randall, S.R., Sherman, D.M., Ragnarsdottir, K.V., 2001. Sorption of As(V) on green rust (Fe_4(II)Fe_2(III)$(OH)_{12}SO_4 \cdot 3H_2O$) and lepidocrocite (γ-FeOOH): surface complexes from EXAFS spectroscopy. Geochim. Cosmochim. Acta 65, 1015–1023.
Scheinost, A.C., Charlet, L., 2008. Selenite reduction by mackinawite, magnetite and siderite: XAS characterization of nanosized redox products. Environ. Sci. Technol. 42, 1984–1989.
Scott, T.B., Allen, G.C., Heard, P.J., Randell, M.G., 2005. Reduction of U(VI) to U(lV) on the surface of magnetite. Geochim. Cosmochim. Acta 69, 5639–5646.
Shuibo, X., Chun, Z., Xinghuo, Z., Jing, Y., Xiaojian, Z., Jingsong, W., 2009. Removal of uranium (VI) from aqueous solution by adsorption of hematite. J. Environ. Radioact. 100, 162–166.
Sun, Y.B., Chen, C.L., Shao, D.D., Li, J.X., Tan, X.L., Zhao, G.X., Yang, S.B., Wang, X.K., 2012a. Enhanced adsorption of ionizable aromatic compounds on humic acid-coated carbonaceous adsorbents. RSC Adv. 2, 10359–10364.
Sun, Y.B., Chen, C.L., Tan, X.L., Shao, D.D., Li, J.X., Zhao, G.X., Yang, S.B., Wang, Q., Wang, X.K., 2012b. Enhanced adsorption of Eu(III) on mesoporous Al_2O_3/expanded graphite composites investigated by macroscopic and microscopic techniques. Dalton Trans. 41, 13388–13394.
Sun, Y.B., Wu, Z.Y., Wang, X.X., Ding, C.C., Cheng, W.C., Yu, S.H., Wang, X.K., 2016a. Macroscopic and microscopic investigation of U(VI) and Eu(III) adsorption on carbonaceous nanofibers. Environ. Sci. Technol. 50, 4459–4467.
Sun, Y.B., Zhang, R., Ding, C.C., Wang, X.X., Cheng, W.C., Chen, C.L., Wang, X.K., 2016b. Adsorption of U(VI) on sericite in the presence of *Bacillus subtilis*: a combined batch, EXAFS and modeling techniques. Geochim. Cosmochim. Acta 180, 51–65.
Sun, Y.B., Lu, S.H., Wang, X.K., 2017a. Plasma-facilitated synthesis of amidoxime/carbon nanofiber hybrids for effective enrichment of ^{238}U(VI) and ^{241}Am(III). Environ. Sci. Technol. 5, 12274–12282.
Sun, Y.B., Wang, X.X., Ai, Y.J., Yu, Z.M., Huang, W., Chen, C.L., Hayat, T., Alsaedi, A., Wang, X.K., 2017b. Interaction of sulfonated graphene oxide with U(VI) studied by spectroscopic analysis and theoretical calculations. Chem. Eng. J. 310, 292–299.
Sylwester, E.R., Hudson, E.A., Allen, P.G., 2000. The structure of uranium (VI) sorption complexes on silica, alumina, and montmorillonite. Geochim. Cosmochim. Acta 64, 2431–2438.
Tang, W., Li, Q., Gao, S., Shang, J.K., 2011. Arsenic (III,V) removal from aqueous solution by ultrafine alpha-Fe2O3 nanoparticles synthesized from solvent thermal method. J. Hazard Mater. 192, 131–138.
Tian, G., Geng, J., Jin, Y., Wang, C., Li, S., Chen, Z., Wang, H., Zhao, Y., Li, S., 2011. Sorption of uranium(VI) using oxime-grafted ordered mesoporous carbon CMK-5. J. Hazard Mater. 190, 442–450.
Wang, P.Y., Wang, X.X., Yu, S.J., Zou, Y.D., Wang, J., Chen, Z.S., Alharbi, N.S., Alsaedi, A., Hayat, T., Chen, Y., Wang, X.K., 2016. Silica coated Fe_3O_4 magnetic nanospheres for high removal of organic pollutants from wastewater. Chem. Eng. J. 306, 280–288.
Wang, P.Y., Yin, L., Wang, J., Xu, C., Liang, Y., Yao, W., Wang, X.X., Yu, S.J., Chen, J., Sun, Y.B., Wang, X.K., 2017a. Superior immobilization of U(VI) and ^{243}Am(III) on polyethyleneimine modified lamellar carbon nitride composite from waste environment. Chem. Eng. J. 326, 863–874.
Wang, T., Zheng, X., Wang, X., Lu, X., Shen, Y., 2017b. Different biosorption mechanisms of uranium(VI) by live and heat-killed *Saccharomyces cerevisiae* under environmentally relevant conditions. J. Environ. Radioact. 167, 92–99.
Worasith, N., Goodman, B.A., Neampan, J., Jeyachoke, N., Thiravetyan, P., 2011. Characterization of modified kaolin from the Ranong deposit Thailand by XRD, XRF, SEM, FTIR and EPR techniques. Clay Miner. 46, 539–559.
Xie, S., Zhang, C., Zhou, X., Yang, J., Zhang, X., Wang, J., 2009. Removal of uranium (VI) from aqueous solution by adsorption of hematite. J. Environ. Radioact. 99, 162–166.
Yang, Y., Chen, T., Zhang, X., Qing, C., Wang, J., Yue, Z., Liu, H., Yang, Z., 2018. Simultaneous removal of nitrate and phosphate from wastewater by siderite based autotrophic denitrification. Chemosphere 199, 130.
Zhang, Z., Liu, H., Lu, P., Chen, T., Ma, W., 2018. Nanostructured α-Fe_2O_3 derived from siderite as an effective Hg(II) adsorbent: performance and mechanism. Appl. Geochem. 96, 92–99.
Zhao, K., Guo, H., 2014. Behavior and mechanism of arsenate adsorption on activated natural siderite: evidences from FTIR and XANES analysis. Environ. Sci. Pollut. Res. 21, 1944–1953.
Zhao, J.H., Liu, J., Li, N., Wang, W., Nan, J., Zhao, Z.W., Cui, F.Y., 2016. Highly efficient removal of bivalent heavy metals from aqueous systems by magnetic porous Fe_3O_4-MnO_2: adsorption behavior and process study. Chem. Eng. J. 304, 737–746.
Zheng, X.Y., Wang, X.Y., Shen, Y.H., Lu, X., Wang, T.S., 2017. Biosorption and biomineralization of uranium(VI) by *saccharomyces cerevisiae*-crystal formation of chernikovite. Chemosphere 175, 161–169.